MATERIALS PHYSICS AND MECHANICS RESEARCH ARTICLE

Submitted: December 12, 2025 **Revised: February 19, 2026** **Accepted: March 25, 2026**

Numerical study of the influence of the reverse martensitic transformation completion degree on the cyclic stability of a shape memory alloy-based actuator

F.S. Belyaev [1]✉, A.E. Volkov [2], D.F. Gorbachenko [1], M.E. Evard [2]

[1] Institute for Problems of Mechanical Engineering RAS, St. Petersburg, Russia

[2] St. Petersburg State University, St. Petersburg, Russia

✉ belyaev_fs@mail.ru

ABSTRACT

Despite all the advantages of shape memory alloy-based actuators, their widespread adoption is hampered by a significant drawback: a gradual decline in performance with repeated actuation. The ways to overcome this drawback are explored. Based on microstructural modeling, the influence of the degree of completion of the reverse martensitic transformation on the operational stability of a torsion actuator with a working body made of a TiNi alloy was investigated. The existence of a critical transformation threshold (~ 75 %) has been identified: exceeding it leads to significant loss of work output, while limiting the transformation to this level ensures practical stabilization of the working cycle parameters. A compromise in the influence of the transformation degree was revealed: reducing it improves the stability of the actuator parameters but reduces the work output per cycle. Based on the obtained results, criteria for selection of an optimal operating mode for actuators intended for long-term cyclic operation were formulated.

KEYWORDS

shape memory alloys • thermomechanical actuator • functional fatigue • martensitic transformations microstructural modeling

Funding. *This work has been supported by the grant of the Russian Science Foundation, RSF 25-21-00361, https://rscf.ru/project/25-21-00361/.*

Citation: Belyaev FS, Volkov AE, Gorbachenko DF, Evard ME. Numerical study of the influence of the reverse martensitic transformation completion degree on the cyclic stability of a shape memory alloy-based actuator. *Materials Physics and Mechanics*. 2026;54(2): 1–16.
http://dx.doi.org/10.18149/MPM.5422026_1

Introduction

Currently, there is active development and implementation of actuators using shape memory alloys (SMA) as working bodies [1–7]. The growing interest in such drives is due, first of all, to increasingly stringent requirements for weight, energy efficiency and reliability of modern advanced systems, such as aircraft, robotic systems and spacecraft. The wide potential of the technology finds practical application in various industries: in aerospace engineering — for controlling structural elements with minimal weight [8–12], in robotics — for creation of powerful and miniature artificial muscles [13–15], in the automotive industry — as actuators for comfort systems and valve mechanisms [16,17], in microelectronics — for precision positioning devices [18,19], and also in medicine — in the development of surgical instruments with controlled deformation [1,20]. The key functional advantages of SMA-based actuators include:

1. High specific force and performance. This property is due to the specific nature of the SMAs, which induces significant reactive stresses and produces useful work through reversible deformation associated with a martensitic transformation. This enables the creation of compact actuators with high power. SMA-based actuators can achieve a weight reduction of up to 80 % compared to conventional electric and hydraulic actuators [21].
2. Structural reliability. High reliability is a consequence of the simple design of such actuators. The absence of complex kinematic units and a small number of moving parts minimize the risk of mechanical failure.
3. Silent operation and low vibration. The smooth nature of SMA deformation ensures almost silent operation and minimal vibration. This makes this technology promising for precision systems, such as optical circuit elements and astronomical instrumentation.
4. Scalability. The physical principles underlying the operation of the SMAs are scale-invariant, which allows them to be successfully applied both in large-scale power drives [12,22] and in microactuators [3,19,23].

The operating principle of a thermomechanical SMA-actuator is based on the eponymous effect – the ability of a material to recover its original shape when heated. Constraining this restoration leads to significant reactive stresses in the material, which enables it to perform useful work. To ensure cyclic operation, the return to the original deformed state upon cooling is achieved by applying an external load. Consequently, the actuator's operating cycle consists of two stages: the cocking stage (accumulation of deformation under load during cooling) and the actuation stage (shape recovery and work output during heating).

Based on their architecture, SMA-actuators are divided into two main types: double-acting and single-acting. Double-acting actuators are capable of generating force in two opposite directions [11,19,24,25]. Typically, this design contains two SMA working bodies, which are alternately heated and cooled. The heated body, restoring its shape, performs a working stroke and simultaneously deforms the other cooled body, thus cocking it for the next cycle. Single-acting actuators perform a working stroke in only one direction [26–32]. This is the most common design, consisting of a SMA working body and an elastic counterbody (e.g., a spring). During the actuation stage, the heated SMA element, overcoming the resistance of the counterbody, restores its shape and performs useful work. At the cocking stage, the cooled working body is deformed by the return force of the elastic counterbody, which has stored energy during the working stroke, thereby closing the thermomechanical cycle.

Despite the listed advantages, SMA-based actuators have a significant drawback that limits their use: instability of the material's functional properties under cyclic loading. During repeated thermomechanical cycling (cocking - actuation), the material exhibits degradation of its characteristics, manifested in the accumulation of residual strain, a shift in the temperatures of the forward and reverse martensitic transformations, and a decrease in the recoverable strain and the developed force [33]. This phenomenon, to varying degrees, is inherent in all SMAs; however, the intensity of degradation is determined by a combination of factors. These include the chemical composition of the alloy, the type of martensitic transformation, the parameters of the preliminary thermomechanical treatment, and the magnitude and nature of the applied load [34–38].

The consequences of property instability are a gradual decrease in work output in the working cycle and incomplete actuation, which can ultimately lead to functional failure.

The main factor responsible for instability of the SMA functional properties is accommodative plastic deformation (microplastic deformation) accompanying the growth of martensite crystals in the austenitic matrix. This process causes irreversible shifts in the crystal lattice, leading to increased macroscopic irreversible deformation. It also generates deformation defects that form internal stress fields. These fields, in turn, have a significant impact on subsequent martensitic transformations.

Experimental research has shown that the final stage of the reverse transformation is responsible for a significant portion of the overall microplastic deformation [39]. Therefore, one method for reducing instability during cyclic actuation is to limit the heating temperature of the working body, which reduces the degree of completion of the reverse martensitic transformation. However, this approach has an obvious drawback: a decrease in the heating temperature leads to a decrease in the generated stresses and, consequently, to a drop in the useful work per cycle. This compromise defines the core objective of this numerical study, which is to explore pathways for enhancing the cyclic stability of the actuator's working cycle without incurring a significant degradation in its performance. To this end, a series of computational experiments was conducted using a microstructural model of SMAs. This model accounts for the accumulation of microplastic deformation, a feature critical for simulating cyclic degradation, and has been successfully applied to actuator simulation problems in prior studies.

Mechanical model of SMA

Due to the complex nature of the SMA deformation behavior, characterized by the absence of a clear relationship between stress, strain, and temperature, mechanical models are required for adequate description of this behavior. There are many different approaches to modeling SMAs, some of which have also been used to describe the operation of SMA actuators [28,30,40–42]. However, to address the objectives of this study, a microstructural model previously developed by the authors [43–48] is used. This model has a key advantage: the ability to correctly account for the main deformation mechanisms of SMA, including the development of microplastic accommodation, which is critical for modeling cyclic degradation. The applied microstructural approach exhibits universality and high predictive ability, as confirmed by its successful application to describe a wide range of phenomena in SMAs, such as fatigue failure [43], transformation and ordinary plasticity [44], deformation during isothermal holding [45], the effect of martensite stabilization [46], as well as heat exchange with the environment [47]. Of particular relevance to the present work is the validation of this model for calculating the work of an SMA specimen under thermomechanical actuator conditions [48]. Thus, the chosen model is a proven tool applicable to solving engineering problems, in particular, for modeling the cyclic operation of SMA-based actuators. Below, the main features of the model and its governing equations, proposed and justified earlier in [49,50], are presented.

Basic model principles.

The model describes the behavior of a representative volume of material, which is considered as a material point. The key principle lies in the multi-level description of the microstructure. The representative volume consists of numerous grains with different crystallographic orientations. Each grain, in turn, can contain austenite and/or several orientational variants of martensite.

According to the Reuss hypothesis, the macroscopic strain of the representative volume ε is calculated as the average over all orientations ω of the strains of individual grains $\varepsilon^{gr}(\omega)$:

$$\varepsilon = \sum_{\omega} f(\omega)\varepsilon^{gr}(\omega), \quad (1)$$

where $f(\omega)$ is the volume fraction of grains with orientation ω.

Kinematics of deformation at the grain level

The strain of an individual grain is represented as the sum of contributions from various physical mechanisms:

$$\varepsilon^{gr} = \varepsilon^{E} + \varepsilon^{T} + \varepsilon^{Ph} + \varepsilon^{MP}, \quad (2)$$

where ε^{E} is elastic strain (according to Hooke's law), ε^{T} is thermal strain (due to thermal expansion), ε^{Ph} is phase strain (associated with the martensitic transformation), ε^{MP} is microplastic strain (associated with plastic accommodation of martensite).

Description of phase transformation

To describe the phase strain, internal variables Φ_n are introduced, where $\frac{\Phi_n}{N}$ represents the volume fraction of the n-th orientational variant of martensite (*N* is the total number of variants). The phase strain of a grain is calculated as the averaged contribution of all martensite variants:

$$\varepsilon^{Ph} = \frac{1}{N}\sum_{n=1}^{N} \Phi_n D^n, \quad (3)$$

where D^n is the Bain strain tensor for the n-th martensite variant.

The condition determining the onset and course of martensitic transformation is formulated through the balance of thermodynamic forces:

$$F_n = \pm F^{fr}, \quad (4)$$

where F_n is the generalized thermodynamic force causing the growth of the n-th variant of martensite, F^{fr} is the dissipative force that prevents the movement of interphase boundaries and causes the presence of temperature-phase hysteresis. The "+" sign in Eq. (4) corresponds to the forward transformation (austenite → martensite), and the "−" sign to the reverse transformation (martensite → austenite).

The thermodynamic forces F_n and F^{fr} are calculated as follows:

$$F_n = \frac{q_0}{T_0}(T - T_0) + \sigma_{ij}: D_{ij}^n - \mu \sum_{m=1}^{N} A_{mn} (\Phi_m - b_m), \quad (5)$$

$$F^{fr} = q_0 \frac{M_s - T_0}{T_0}. \quad (6)$$

The first expression follows from the Gibbs potential and the second follows from the condition of the onset of direct martensitic transformation at temperature M_s. In these expressions q_0 is the latent heat of transformation, T_0 is the temperature of thermodynamic phase equilibrium (austenite and martensite), *T* is the temperature of the

representative volume, σ is applied stress, b is the density of oriented defects, A is the matrix that determines the interaction of martensite variants described in detail in [49,50]. The coefficient μ and the equilibrium temperature T_0 depend on the material constants and can be calculated as follows:

$$\mu = -\frac{q_0(M_s - M_f)}{T_0(1-2\alpha)}, \quad (7)$$

$$T_0 = \frac{M_s + A_f}{2}, \quad (8)$$

where M_f and A_f are the finish temperatures of the forward and reverse martensitic transformations respectively, α is a material constant characterizing the coherency of the martensitic phases. The choice of the value of μ in the form (7) follows from the condition that the direct martensitic transformation is completed at the temperature M_f upon cooling under no load.

Description of martensite reorientation.

The reorientation (twinning) of martensite is described using a specialized approach. This process is interpreted as a shift within the space of internal variables $\Phi_1, \cdots, \Phi_N$, under the constraint that the total volume fraction of martensite Φ^{gr} remains constant. The following hypotheses are postulated:

1. Any variant of martensite can transform into any other variant.
2. Reorientation proceeds in the direction within the space $\Phi_1, \cdots, \Phi_N$ that corresponds to the steepest decrease of the Gibbs potential G.
3. Reorientation is initiated when the thermodynamic driving force reaches a critical value.

To find the direction of reorientation we use vector $\tilde{F}$:

$$\tilde{F} = \left\{-\frac{\partial G}{\partial \Phi_1}, \cdots, -\frac{\partial G}{\partial \Phi_N}\right\}. \quad (9)$$

The projection L of a vector $\tilde{F}$ onto the plane $\Phi_1 + \cdots + \Phi_N = \text{const}$ corresponds to the direction of the steepest decrease of the Gibbs potential during reorientation. However, moving in this direction may violate the geometrical constraints requiring the non-negativity of volume fractions. To address this issue, if for some component n we have $\Phi_n = 0$ and $L_n < 0$, we replace L with its projection L' onto the intersection of the planes defined by $\Phi_n = 0$ and $\Phi_1 + \cdots + \Phi_N = \text{const}$. This procedure is repeated for other components of L as necessary. Finally, after normalizing the resulting vector, we obtain the unit direction l. This direction satisfies the hypothesis 2 and ensures that the conditions $\Phi^{gr} = \text{const}, \Phi_n \geq 0, \ n = 1, \ldots, N$ are not violated.

In accordance with the hypothesis 3, the condition for the onset of reorientation in the direction l is postulated as:

$$F^{tw}(l) = F^{frtw}, \quad (10)$$

where F^{frtw} is a material constant representing the critical force required to initiate reorientation, $F^{tw}(l)$ is the thermodynamic driving force for reorientation, defined by the directional derivative of the Gibbs potential:

$$F^{tw}(l) = -\frac{\partial G}{\partial l} = -\sum_{n=1}^{N} l_n \frac{\partial G}{\partial \Phi_n} = N \sum_{n=1}^{N} l_n \tilde{F}_n, \quad (11)$$

where $\tilde{F}_n$ denotes the thermodynamic force conjugate to the internal variable Φ_n.

It follows from hypotheses 1 and 2 that the increments $d\Phi_n$ are proportional to the components l_n:

$$d\Phi_n = l_n d\phi, \quad (12)$$

where $d\phi$ is a proportionality factor to be determined from condition (10).

Accounting for microplastic deformation

The growth of a martensite crystal causes deformation incompatibility with the surrounding austenite matrix and with crystallographically non-corresponding martensite variants, generating internal stresses and, consequently, microplastic slip. A key assumption in describing this deformation mechanism is that the microplastic deformation associated with the growth of a particular martensite variant is proportional to its Bain strain deviator:

$$\varepsilon^{MP} = \frac{1}{N}\sum_{n=1}^{N} \kappa \varepsilon_n^{mp} dev(D^n), \quad (13)$$

where ε_n^{mp} is the scalar measure of microplastic deformation associated with the growth of the n-th martensite variant, κ is a scaling coefficient.

To calculate the values of ε_n^{mp}, microplastic flow conditions are introduced into the model. These conditions are similar to the condition of plastic flow in the one-dimensional case, taking into account kinematic (translational) and isotropic hardening, where the role of stress is played by the generalized thermodynamic force F_n^p, and the kinematic and isotropic hardening correspond to the thermodynamic forces F^y and F_n^ρ:

$$\left|F_n^p - F_n^\rho\right| = F^y, \ \left(F_n^p - F_n^\rho\right) dF_n^p > 0. \quad (14)$$

The generalized thermodynamic force causing microplastic deformation is calculated as follows:

$$F_n^p = \mu \sum_{m=1}^{N} A_{mn}(\Phi_m - b_m). \quad (15)$$

Evolution of defects and hardening

Microplastic deformation causes material hardening through the generation of deformation-induced defects. While many types of defects exist, accounting for each individually is impractical. To simplify, all deformation-induced defects are classified into two types depending on whether they create long-range oriented internal stress fields: oriented defects, which produce such fields, and scattered defects, which do not.

The growth of the n-th martensite variant generates specific defects (e.g., dislocations on certain slip planes) that create internal stress fields with a distinct orientation. Consequently, the model distinguishes the densities of oriented defects, $b_1, \ldots, b_N$, produced by each martensite variant. The increase in the density b_n is assumed to be proportional to the microplastic strain ε_n^{mp} caused by the growth of the n-th martensite variant. However, this density cannot grow indefinitely. As microplastic deformation intensifies, the density is reduced by the annihilation of dislocations at grain boundaries. We assume that the generation of new defects and their annihilation eventually reach equilibrium, defining a maximum density β^*. This saturation behavior is described by the following equation:

$$\dot{b_n} = k_b \left(\dot{\varepsilon}_n^{mp} - \frac{|b_n|}{\beta^*} \dot{\varepsilon}_n^{mp} H\left(b_n \dot{\varepsilon}_n^{mp}\right) \right), \quad (16)$$

where *H* is the Heaviside function, k_b is a scaling factor. In this equation the first term in parentheses represents defect generation and the second term represents annihilation at the grain boundary.

In contrast, scattered defects generated by microplastic deformation are qualitatively indistinguishable regardless of which martensite variant caused the deformation. They are therefore described by a single scalar density *f*. This density is assumed to be proportional to the total accumulated microplastic strain from all variants. Furthermore, the density of scattered defects can decrease over time due to thermally activated processes. This evolution is governed by the following equation:

$$\dot{f} = \sum_{m=1}^{N} |\dot{\varepsilon}_m^{mp}| + r_0 e^{-\frac{U_f}{kT}} (f - f_0), \quad (17)$$

where r_0 is the recovery coefficient, U_f is the activation energy, k is the Boltzmann constant, f_0 is the equilibrium density of scattered defects.

To obtain a closed system of equations, it is necessary to introduce hardening laws. The model assumes that scattered defects impede dislocation movement, thereby increasing the yield stress. Consequently, their density is related to isotropic hardening. Clusters of oriented defects create internal stress fields, the effect of which is combined with external stress, shifting the center of the yield surface. Consequently, their density is related to kinematic hardening. Linear dependencies are proposed to relate hardening to defect densities:

$$F_n^{\rho} = a_{\rho} b_n, \quad (18)$$

$$F^{y} = a_y f, \quad (19)$$

where a_{ρ} and a_y are material constants determining the intensity of the corresponding types of hardening.

Computational algorithm

The model describes the behavior of a representative volume subjected to external thermomechanical loading. The input (control) parameters are stress σ, temperature *T*, and time *t*; the outputs are the macroscopic strain and the evolution of the internal variables.

The simulation procedure is divided into stages, each corresponding to an interval of monotonic variation of the control parameters. Within each stage, the system of evolution equations is integrated numerically. If the boundary conditions are prescribed in terms of strain (or as a stress-strain relationship, e.g., to account for the counterbody stiffness) rather than stress, the stress at the stage is determined iteratively to satisfy the required strain.

Each stage is further subdivided into increments (in time or another control parameter). For a given increment, the algorithm proceeds as follows:

1. The increments of all control parameters $\Delta\sigma, \Delta T, \Delta t$ are computed.
2. The thermodynamic driving forces F_n are evaluated using Eq. (5), and the martensitic transformation criteria (4) are checked. If the criteria are met, the changes in martensite volume fractions $\Delta\Phi_n^{tr}$ are calculated.
3. The reorientation driving force F^{tw} is calculated using Eq. (11), and the reorientation condition (10) is verified. If it is active, the contribution of reorientation to the changes in martensite volume fractions $\Delta\Phi_n^{tw}$ are computed.

4. Using the updated volume fractions, i.e., $\Phi_n + \Delta\Phi_n^{tr} + \Delta\Phi_n^{tw}$, the driving forces for microplastic strain F_n^p are calculated from Eq. (15), and the flow conditions (14) are evaluated. For all active flow systems, a system of equations is solved, comprising the flow conditions (14), the evolution equations for defect densities (16)–(17), and the hardening relations (18)–(19). The solution gives the corresponding increments of microplastic strain $\Delta\varepsilon_n^{mp}$, defect densities Δb_n, Δf, and hardening variables ΔF_n^{ρ}, ΔF^{y}.
5. The total grain strain ε^{gr} is then calculated using Eqs. (2), (3) and (13).
6. Steps 2 through 5 are performed independently for each grain. Finally, the averaged strain of the representative volume ε is obtained using Eq. (1).

The proposed algorithm numerically captures the essential features of the mechanical behavior of shape memory alloys required for the analysis of actuator applications.

Actuator

Schematic of the actuator

The object of this study is a single-acting torsion actuator. Its design (Fig. 1) comprises a working element (a rod made of a TiNi alloy), connected in series with an elastic counterbody (a return spring). Upon actuation, the working rod restores its shape, generating a torque that rotates a lever fixed to its end.

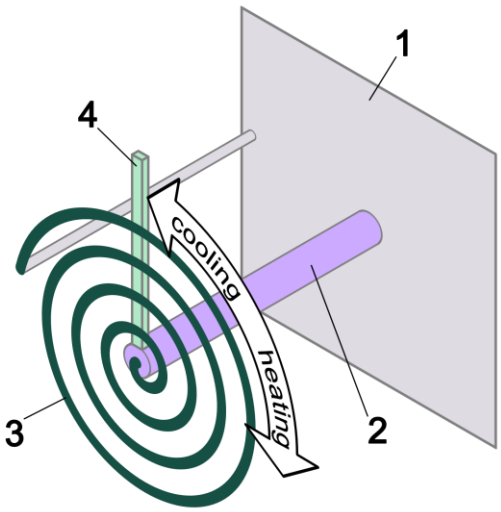

Fig. 1. Schematic diagram of the single-acting torsion actuator. Key components: 1 – base frame; 2 – SMA working body (TiNi rod); 3 – elastic counterbody (spring); 4 – output lever

System parameters

The TiNi alloy was selected as the working body material owing to its status as a widely used SMA and the combination of high functional properties, which include a significant recoverable strain. For the numerical simulation, the set of material constants given in Table 1 was adopted. This set, originally calibrated in [48], was validated against experimental data for actuators with elastic counterbodies of varying stiffness [33], confirming its adequacy for the present study.

Table 1. Material constants for TiNi alloy

Material constant	Symbol	Value
Number of martensite variants	N	12.00
Latent heat (enthalpy) of the direct martensitic transformation, MJ/m^3	q_0	-160.00
Characteristic temperatures of martensite transformation, K	M_f M_s A_s A_f	310.00 332.00 340.00 363.00
Temperature of the thermodynamic equilibrium, K	T_0	347.50
interaction coefficient of martensite variants	α	0.20
Microplastic strain scaling factor	κ	1.00
Coefficient of isotropic hardening, MPa	a_y	1.00
Coefficients of kinematic hardening, MPa	a_p	10.00
Maximum value of the oriented defects density	β^*	0.60
Oriented defects scaling factor	k_b	2.00
Initial value of scattered defects	f_0	0.00
Scattered defects recovery coefficient	r_0	0.09
Activation energy, kJ/mol	U_f	40.00

The counteraction is provided by an elastic counterbody; therefore, the increment in strain upon heating $\Delta\gamma$ is proportional to the increase in stress $\Delta\tau$. Hence, one may write $\Delta\tau = K \cdot \Delta\gamma$, where K is the linear coefficient characterizing the stiffness of the counterbody. In this work, the coefficient K was set to 11.3 GPa. This value is optimal for the actuator configuration under consideration, as it corresponds to the maximum work output per cycle, a finding established in prior research [33,48].

Working cycle

The working cycle of the actuator is based on the ability of a pre-deformed SMA element to recover its original shape upon heating due to the shape memory effect. Consequently, the actuator requires a preparatory step to introduce an initial deformation into the working body. A schematic of the preparation procedure and the subsequent working cycle is presented in Fig. 2.

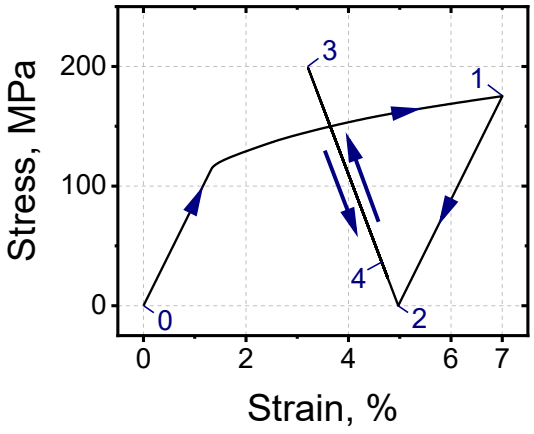

Fig. 2. Schematic of the initial preparation of the actuator's working body via torsional deformation (0–1) and unloading (1–2), followed by the working cycle consisting of the working stroke during heating (2–3) and the cocking phase during cooling (3–4)

The preparation of the TiNi working rod was simulated according to the following sequence. First, at the point (0), the rod is in a fully martensitic state. This state is achieved by cooling the unstressed rod from the austenitic state to a temperature below the martensite finish temperature M_f. Under such stress-free cooling conditions, the martensite forms in a self-accommodated manner, meaning that all variants are present in nearly equal volume fractions. From this initial state, the rod was subjected to torsional loading up to a shear strain of 7 % (segment 0–1). During this stage, the martensite variants undergo reorientation: those variants whose Bain strain is the most aligned with the applied stress grow at the expense of others, increasing their volume fraction. This process results in a textured martensitic structure. The rod was then unloaded (segment 1–2). The unloading is purely elastic, meaning that the reoriented martensite structure remains unchanged, leaving a residual strain of approximately 5 %. The prepared rod was subsequently installed in the actuator assembly with one end rigidly fixed and the other connected to the elastic counterbody (spring), after which the system was ready for cyclic operation.

The working cycle consists of two phases. During the working stroke (2–3), the working body is heated. When the temperature rises above the reverse transformation start temperature, A_s, the martensite begins to transform into austenite. As a result, the rod starts to recover its shape due to the shape memory effect, inducing a rising mechanical stress in the system by working against the elastic counterbody. During the subsequent cocking phase (3–4), the working body is cooled. The austenite formed in the previous stage now begins to transform back into martensite. However, since this transformation occurs under the stress applied by the pre-strained spring, the martensite formed is oriented, with preferential selection of variants whose orientations are aligned with the spring-induced stress. Consequently, the rod deforms back towards state 2, resulting in a drop in stress (usually not to zero). After completing the cocking phase, the actuator is reset for the next cycle. In stress-strain coordinates, the trajectory of the cycle follows along a straight line whose slope is defined by the stiffness of the elastic counterbody.

Simulation results

The actuator produces work output during the working stroke. The magnitude of this work is directly dependent on the heating temperature, reaching its maximum when the reverse martensitic transformation is complete. The objective of this study is to investigate the potential for enhancing the stability of the actuator's parameters by intentionally limiting the degree of reverse transformation completion. To this end, a series of numerical experiments simulating working cycles with incomplete transformation was conducted. Four heating temperatures were chosen, corresponding to work output levels of 90, 75, 50, and 25 % of the work produced in the first cycle with full reverse transformation. This approach enables a quantitative evaluation of the influence of transformation degree on the characteristic degradation. In all simulated cases, cooling was modeled until complete transformation to the martensitic state.

The simulation results for the first 15 cycles demonstrate a degradation of the actuator's key functional characteristics with an increasing number of cycles in all

regimes. This is evidenced by a simultaneous reduction in both the maximum cycle stress (Fig. 3(a)) and the magnitude of recoverable shape memory strain (Fig. 3(b)). Given that the specific work of the actuator is governed by the product of these parameters, their simultaneous decline leads to a corresponding drop in the work per cycle (Fig. 4, solid symbols).

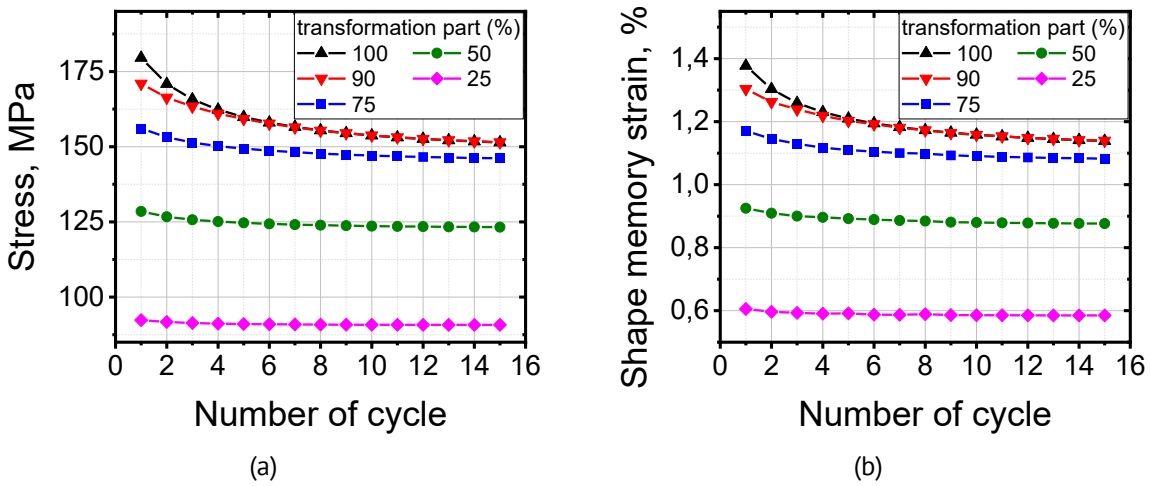

Fig. 3. Evolution of the maximum cycle stress (a) and shape memory strain (b) with the number of cycles for different degrees of reverse transformation completion

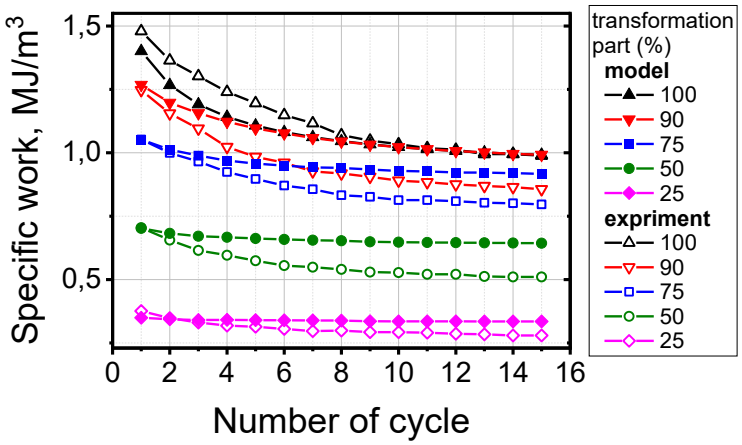

Fig. 4. Specific work per cycle on the cycle number for different degrees of reverse transformation completion. Simulation results (solid symbols) and experimental data from [51] (open symbols)

A clear dependence of the degradation dynamics on the degree of reverse transformation completion was identified. When the transformation is limited to 50 and 25 % of the maximum value, the actuator exhibits high stability, with the specific work remaining nearly constant. In contrast, regimes with complete (100 %) and near-complete (90 %) transformation are characterized by intense degradation: the work output declines rapidly, and by the 15-th cycle its value approaches the value of the 75 %-transformation regime. This observed trend is in qualitative agreement with the experimental data reported in [51], shown for comparison in Fig. 4 (open symbols).

Following the validation of the model against experimental data, a predictive simulation of the actuator's operation over 100 cycles was conducted for the same heating levels. The obtained dependences of the specific work per cycle on the cycle number are presented in Fig. 5. The analysis reveals two distinct stages of performance degradation:

1. Initial stage (up to ~ 30 cycles): characterized by a rapid but gradually slowing decrease in the work output.
2. Steady-state degradation stage (beyond 30 cycles): marked by a linear decrease in the work output.

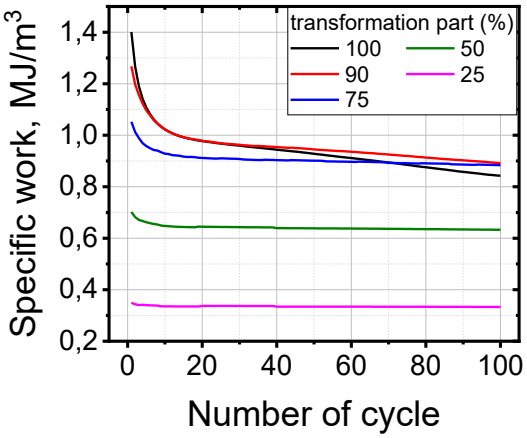

Fig. 5. Specific work per cycle on the cycle number for varying reverse transformation completion levels

The decisive influence of transformation completeness on long-term stability is evident. For regimes with complete (100 %) and near-complete (90 %) transformation, the slope in the second stage remains large, indicating a significant continued decline in performance. In contrast, for regimes with a transformation degree of 75 % or lower, the curves in the second stage become almost horizontal, exhibiting only a slight slope. This indicates a transition to a quasi-stable operating state with minimal gradual degradation of performance.

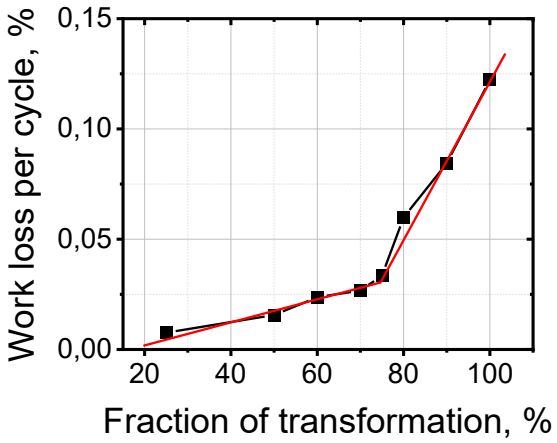

Fig. 6. Specific work loss per cycle in the steady-state degradation regime as a function of the reverse transformation fraction. The bilinear approximation reveals a critical transition near 75 % completion

To quantify the boundary between stable and unstable operational regimes, additional calculations were performed for various heating limits. Based on these results, a dependence of the work loss per cycle during the steady-state degradation stage on the reverse transformation fraction was obtained (Fig. 6). This dependence is well approximated by a bilinear function with a breakpoint near 75 %, which quantitatively confirms the previously identified transition.

Based on the simulation results, the following practical recommendations for actuators intended for long-term cyclic operation are proposed:

1. To ensure long-term parameter stability, it is recommended to select an operating cycle with a reverse transformation degree not exceeding 75 %. The predictive modeling results (Figs. 5 and 6) demonstrate that exceeding this threshold leads to a significantly higher degradation rate. For instance, with complete transformation, the work output falls below that of the 75 % regime after only ~ 70 cycles; for a 90% transformation, this occurs after ~ 100 cycles. Consequently, the higher initial work output in the early cycles is negated by its accelerated decline.
2. During the design phase, the performance loss over the actuator's target service life must be estimated. This assessment should account for the linear degradation in the steady-state regime to guarantee that the work output remains above the minimum required threshold.
3. The significant performance drop during the initial cycling stage (approximately the first 30 cycles) must be considered. To mitigate this problem in practice, it is recommended to conduct thermal cycling (training) of the working element before use.

For a comparative overview of the actuator's performance across the studied thermal regimes, Table 2 summarizes the key quantitative metrics: the work output in the first cycle, the cumulative work loss during the initial cycling stage (cycles 1 – 30), and the specific work loss per cycle in the steady-state regime.

Table 2. Actuator's work output and its degradation across simulated thermal regimes

Part of reverse transformation, %	Specific work at the first cycle, MJ/m^3	Work loss in the Initial stage of degradation, %	Work loss per cycle in the stage of steady-state degradation, %
100	1.401	31.5	0.122
90	1.268	24.1	0.084
80	1.122	16.1	0.06
75	1.052	13.7	0.033
70	0.977	12.8	0.027
60	0.834	9.8	0.024
50	0.702	8.4	0.016
25	0.349	3.5	0.0076

Conclusions

1. Microstructural modeling has identified accommodative microplastic deformation, predominantly occurring at the final stage of the reverse martensitic transformation, as the primary mechanism behind the degradation of key functional characteristics (maximum stress, recoverable strain, and specific work) in SMA-based thermomechanical actuators under cyclic loading.

2. The long-term degradation process exhibits two distinct stages: an initial stage (up to ~ 30 cycles) with rapid, non-linear deterioration of parameters, followed by a steady-state stage characterized by a linear decrease in specific work.
3. A critical threshold for the degree of completion of the reverse martensitic transformation has been quantitatively established at approximately 75 %. Exceeding this threshold leads to intense degradation, including during the steady-state stage. Conversely, limiting the transformation to 75 % or less enables an operational regime with minimal parameter instability.
4. A fundamental compromise between performance and stability has been demonstrated. While reducing the degree of transformation completion enhances cycle-to-cycle stability by decreasing the relative work loss, at the same time it reduces the absolute work output per cycle.

Based on these findings, the following practical guidelines for designing stable SMA actuators for long-term cycling are proposed:
1. Adopt an operating regime with a degree of reverse transformation not exceeding 75 %.
2. Account for performance losses during the initial cycling stage (first ~ 30 cycles), which can be mitigated by thermal cycling (training) of the working element before use.
3. Perform a service life prediction based on the linear degradation rate observed in the steady-state regime to ensure that the work output remains above the required minimum throughout the operational lifetime.

CRediT authorship contribution statement

Fedor S. Belyaev: conceptualization, investigation, writing – original draft; **Aleksandr E. Volkov**: writing – review & editing, supervision; **Daniil F. Gorbachenko**: investigation; **Margarita E. Evard**: writing – review & editing, supervision.

Conflict of interest

The authors declare that they have no conflict of interest.

References

1. Gangil N, Siddiquee AN, Maheshwari S. Towards applications, processing and advancements in shape memory alloy and its composites. *Journal of Manufacturing Processes.* 2020;59: 205–222.
2. Kim M, Heo J, Rodrigue H, Lee H, Pané S, Han M, Ahn SH. Shape Memory Alloy (SMA) Actuators: The Role of Material, Form, and Scaling Effects. *Advanced Materials.* 2023;35(33): 2208517.
3. Kohl M. *Shape Memory Microactuators.* Berlin: Springer; 2004.
4. Mertmann M, Vergani G. Design and application of shape memory actuators. *The European Physical Journal Special Topics.* 2008;158(1): 221–230.
5. Mohd Jani J, Leary M, Subic A, Gibson MA. A review of shape memory alloy research, applications and opportunities. *Materials & Design.* 2014;56: 1078–1113.
6. Mohd Jani J, Leary M, Subic A. Designing shape memory alloy linear actuators: A review. *Journal of Intelligent Material Systems and Structures.* 2017;28(13): 1699–1718.
7. Yadav SK. Shape Memory Alloy Actuators: A Review. *IJRASET.* 2019;7(5): 799–802.
8. Ameduri S, Concilio A. A shape memory alloy torsion actuator for static blade twist. *Journal of Intelligent Material Systems and Structures.* 2019;30(17): 2605–2626.

9. Hartl DJ, Lagoudas DC. Aerospace applications of shape memory alloys. *Proceedings of the Institution of Mechanical Engineers, Part G: Journal of Aerospace Engineering.* 2007;221(4): 535–552.
10. Liu R, Zhang C, Ji H, Zhang C, Qiu J. Training, Control and Application of SMA-Based Actuators with Two-Way Shape Memory Effect. *Actuators.* 2023; 12(1): 25.
11. Yang J, Zhang Y, Gu X, Li J, Fang P, Yang X, et al. Bi-direction and flexible multi-mode morphing wing based on antagonistic SMA wire actuators. *Chinese Journal of Aeronautics.* 2024;37(12): 373–387.
12. Nam C, Chattopadhyay A, Kim Y Application of shape memory alloy (SMA) spars for aircraft maneuver enhancement. In: *Proc. SPIE 4701, Smart Structures and Materials 2002: Smart Structures and Integrated Systems.* 2002. p.226–236.
13. Kheirikhah MM, Rabiee S, Edalat ME. A Review of Shape Memory Alloy Actuators in Robotics. In: Ruiz-del-Solar J, Chown E, Plöger PG. (Eds.) *RoboCup 2010: Robot Soccer World Cup XIV.* Berlin: Springer; 2011. p.206–217.
14. Lu Y, Xie Z, Wang J, Yue H, Wu M, Liu Y. A novel design of a parallel gripper actuated by a large-stroke shape memory alloy actuator. *International Journal of Mechanical Sciences.* 2019;159: 74–80.
15. Sreekumar M, Nagarajan T, Singaperumal M, Zoppi M, Molfino R. Critical review of current trends in shape memory alloy actuators for intelligent robots. *Industrial Robot.* 2007;34(4): 285–294.
16. Jani JM, Leary M, Subic A. Shape Memory Alloys in Automotive Applications. *Applied Mechanics and Materials.* 2014;663: 248–253.
17. Stoeckel D. Shape Memory Actuators for Automotive Applications. *Materials & Design.* 1990;11(6): 302–307.
18. Liu Q, Ghodrat S, Huisman G, Jansen KMB. Shape memory alloy actuators for haptic wearables: A review. *Materials & Design.* 2023;233: 112264.
19. Xu J, Kimura Y, Tsuji K, Abe K, Shimizu T, Hasegawa H, Mineta T. Fabrication and characterization of SMA film actuator array with bias spring for high-power MEMS tactile display. *Microelectronic Engineering.* 2020;227: 111307.
20. Hamid QY, Wan Hasan WZ, Azmah Hanim MA, Nuraini AA, Hamidon MN, Ramli HR. Shape memory alloys actuated upper limb devices: A review. *Sensors and Actuators Reports.* 2023;5: 100160.
21. Kamlet M. *NASA tests new alloy to fold wings in flight - NASA*. Available from: https://www.nasa.gov/centers/armstrong/feature/nasa-tests-new-alloy-to-fold-wings-in-flight.html [Accessed 30th November 2025].
22. Park HB, Kim DR, Kim HJ, Wang W, Han MW, Ahn SH. Design and Analysis of Artificial Muscle Robotic Elbow Joint Using Shape Memory Alloy Actuator. *Int J Precis Eng Manuf.* 2020;21(2): 249–256.
23. Liu Q, Wang W, Reynolds MF, Cao MC, Miskin MZ, Arias TA, Muller DA, McEuen PL, Cohen I. Micrometer-sized electrically programmable shape-memory actuators for low-power microrobotics. *Science Robotics.* 2021;6(52): eabe6663.
24. Priadko AI, Pulnev SA, Nikolaev VI, Rogov AV, Shmakov OA, Golyandin SN, Chikiryaka AV. Investigation of single crystal Cu-Al-Ni alloy bending force elements for linear motors. *Materials Physics and Mechanics.* 2016;29(2): 158–165.
25. Pei YC, Wang XY, Yao ZY, Wang BH, Liao Z hui, Lu H. The driving characteristics of bidirectional SMA wire actuators - Theoretical modeling and experimental testing. *Sensors and Actuators A: Physical.* 2024;372: 115328.
26. Movchan AA, Ekster NM. Actuator with a series connection of a shape memory alloy's rod and an elastic bias element. *Journal on Composite Mechanics and Design.* 2021;27(2): 169–190. (In Russian)
27. Movchan AA, Ekster NM. Selection of materials for creating bias bodies in force actuator with a working body made of a shape memory alloy. Part 1. Metal bias bodies. *Journal on Composite Mechanics and Design.* 2025;31(3): 351–372.
28. Khan AM, Bijalwan V, Shin B, Kim Y. Adaptive Neural Network Control Design and Analysis for Sma Actuators Having Dominant Shape Memory Effect. [Preprint] 2023. Available from: https://www.ssrn.com/abstract=4577203 [Accessed 30th November 2025].
29. Khan AM, Bijalwan V, Shin B, Kim Y. Adaptive neural network controller for the rotating SMA actuator. *Sensors and Actuators A: Physical.* 2024;370: 115240.
30. Mohd Jani J, Huang S, Leary M, Subic A. Numerical modeling of shape memory alloy linear actuator. *Computational Mechanics.* 2015;56: 443–461.
31. Ostropiko E, Razov A, Cherniavsky A. Investigation of TiNi shape memory alloy for thermosensitive wire drive. *MATEC Web Conf.* 2015;33: 03021.
32. Ostropiko ES, Razov AI. Functional properties of TiNi conical workingelements in the holding and release device. *Cybernetics and Physics.* 2018;7: 216–219.
33. Sibirev A, Belyaev S, Resnina N. The influence of counter-body stiffness on working parameters of NiTi actuator. *Sensors and Actuators A: Physical.* 2021;319: 112568.
34. Belyaev S, Resnina N, Zhuravlev R. Deformation of Ti–51.5at.%Ni alloy during thermal cycling under different thermal-mechanical conditions. *Journal of Alloys and Compounds.* 2013;577: S232–S236.

35. Furuya Y, Park YC. Thermal cyclic deformation and degradation of shape memory effect in Ti-Ni alloy. *Nondestructive Testing and Evaluation.* 1992;8–9(1–6): 541–554.
36. Hamilton RF, Sehitoglu H, Efstathiou C, Maier HJ. Mechanical response of NiFeGa alloys containing second-phase particles. *Scripta Materialia.* 2007;57: 497–499.
37. Morgan NB, Friend CM. A review of shape memory stability in NiTi alloys. *J. Phys. IV France.* 2001;11(PR8): Pr8-325-Pr8-332.
38. Sehitoglu H, Wu Y, Patriarca L. Shape memory functionality under multi-cycles in NiTiHf. *Scripta Materialia.* 2017;129: 11–15.
39. Sibirev A, Belyaev S, Resnina N. Softening process during reverse martensitic transformation in TiNi shape memory alloy. *Journal of Alloys and Compounds.* 2016;661: 155–160.
40. Movchan AA, Ekster NM. Geometrically Nonlinear Analysis of the Operation of a Shape Memory Alloy Force Actuator. *Russ Metall.* 2025;2025(4): 717–726.
41. Movchan AA, Ekster NM. Theoretical Analysis of the Operation of a Force Actuator with a Working Body Consisting of a Shape Memory Alloy Rod and an Elastic Displacement Body. *Russ Metall.* 2023;2023(4): 389–397.
42. Mirzaeifar R, Elahinia MH. Mathematical Modeling and Simulation. In: Elahinia MH. (Ed.) *Shape memory alloy actuators: design, fabrication, and experimental evaluation.* Wiley; 2015. p.45–84.
43. Belyaev FS, Evard ME, Volkov AE. Microstructural modeling of fatigue fracture of shape memory alloys at thermomechanical cyclic loading. *AIP Conference Proceedings.* 2018;1959: 070003.
44 Belyaev FS, Evard ME, Volkov AE. Simulation of the plastic deformation of shape memory alloys considering shear anisotropy on the slip plane. *Materials Physics and Mechanics.* 2023;51(1): 61–67.
45. Resnina N, Ivanov A, Belyaev F, Volkov A, Belyaev S. Simulation of recoverable strain variation during isothermal holding of the $Ni_{51}Ti_{49}$ alloy under various regimes. *Letters on Materials.* 2023;13(1): 33–38.
46. Volkov AE, Belyaev FS, Volkova NA, Vukolov EA, Evard ME, Rebrov TV. The effect of martensite stabilization in titanium nickelide after various methods of pre-deformation: simulation with a single set of constants. *Materials Physics and Mechanics.* 2024;52(4): 91–99.
47. Belyaev F, Volkov AE, Vukolov E, Evard M, Kudrina KV, Starodubova M. Influence of latent heat and heat exchange conditions on tension behavior of shape memory alloy specimen. *Materials Physics and Mechanics.* 2024;52(5): 18–28.
48. Belyaev FS, Volkov AE, Gorbachenko DF, Evard ME. Modeling of working cycles of thermomechanical actuators based on shape memory alloys at repeated actuation. *Materials Physics and Mechanics.* 2024;52(6): 89–90.
49. Belyaev F, Evard M, Volkov A, Volkova N. A Microstructural Model of SMA with Microplastic Deformation and Defects Accumulation: Application to Thermocyclic Loading. *Materials Today: Proceedings.* 2015;2: S583–S587.
50. Volkov AE, Belyaev FS, Evard ME, Volkova NA. Model of the Evolution of Deformation Defects and Irreversible Strain at Thermal Cycling of Stressed TiNi Alloy Specimen. *MATEC Web of Conferences.* 2015;33: 03013.
51. Sibirev A, Belyaev S, Resnina N. Improvement of the NiTi actuator performance stability by decreasing its operating temperature range. *Sensors and Actuators A: Physical.* 2023;363: 114743.